

Ensemble-Based Analysis of Errors in Atmospheric Profiles Retrieved from GNSS Occultation Data

A. K. Steiner and G. Kirchengast

Institute for Geophysics, Astrophysics, and Meteorology (IGAM), University of Graz,
Austria
andi.steiner@uni-graz.at

Abstract. We present results of an empirical error analysis based on simulated GNSS radio occultation data. Occultation observations were simulated for one day adopting the planned European weather satellite METOP as Low Earth Orbit satellite and its GNSS Receiver for Atmospheric Sounding as sensor. An ensemble of 300 occultation events with 100 events in each of three latitude bands (low, middle, high) was chosen and excess phase path profiles were computed involving quite realistic atmospheric modeling and observation system modeling. The rms error of the ionosphere corrected phase path profile sampled at 10 Hz was found to be 2–3 mm, at meso- and stratospheric heights, and the atmospheric Doppler error to be ~ 3 mm/sec, mimicking realistically modern receiver performance. Atmospheric profiles were retrieved by applying an advanced geometric optics bending angle retrieval algorithm followed by Abelian refractivity retrieval and, subsequently, by dry air retrieval in the stratosphere and optimal estimation retrieval in the troposphere. The retrieved profiles were referenced to the “true” co-located ones of the ECMWF analysis field used as atmospheric model. Based on these data, we empirically estimated bias profiles and covariance matrices (standard deviations and correlation functions) for the retrieval products bending angle, refractivity, pressure, geopotential height, temperature and specific humidity. Specific results include: Refractivity exhibits a relative standard deviation of 0.1–0.75% and a relative bias of $<0.1\%$ at 5–40 km height. Temperature shows a standard deviation of 0.2–1 K at 3–31 km height and a bias of <0.5 K below 33 km and of <0.1 K below 20 km. The obtained empirical errors are conservative error estimates and provide a valuable basis for further retrieval algorithm improvements and for proper specification of observational errors in data assimilation systems.

1 Introduction

Radio occultation observations based on Global Navigation Satellite System (GNSS) signals have great potential to globally provide key climate variables with high accuracy in the troposphere and stratosphere. High quality atmospheric profiles could support the advancement of climate monitoring and modeling as well as the improvement of numerical weather prediction and atmospheric analysis via data assimilation schemes.

We performed an ensemble-based empirical analysis of errors in order to provide complete error information on profiles retrieved from GNSS occultation data as needed, e.g., by data assimilation schemes. The study is based on an end-to-end

forward-inverse simulation involving quite realistic neutral atmosphere and ionosphere modeling and realistic simulation of radio occultation observations (Sect. 2), forward modeling of excess phase observables including observation system error modeling (Sect. 3), and retrieval of atmospheric parameters (Sect. 4). The error analysis scheme is described in Sect. 4 as well. Results on the error statistics comprising biases, standard deviations, and correlation functions are presented and discussed in Sect. 5 with focus on refractivity and temperature errors. Conclusions of our findings are drawn in Sect. 6.

2 Ensemble Design and Simulations

Simulation of the data set was carried out with the End-to-end GNSS Occultation Performance Simulator EGOPS4 (Kirchengast 1998; Kirchengast et al. 2002).

Occultation observations were simulated for one day, September 15, 1999, adopting the planned European METOP platform as Low Earth Orbit (LEO) satellite and its GNSS Receiver for Atmospheric Sounding (GRAS) as sensor. The nominal 24-satellite Global Positioning System (GPS) was employed as transmitter system, taking rising and setting occultation events into account. We chose an ensemble of 300 events out of 574 events obtained in total, which are equally distributed in space and time with 100 events in each of three latitude bands, low (-30° to $+30^\circ$), middle ($\pm 30^\circ$ to $\pm 60^\circ$), and high ($\pm 60^\circ$ to $\pm 90^\circ$) latitudes. Figure 1 illustrates the event distribution of this ensemble of 300 profiles.

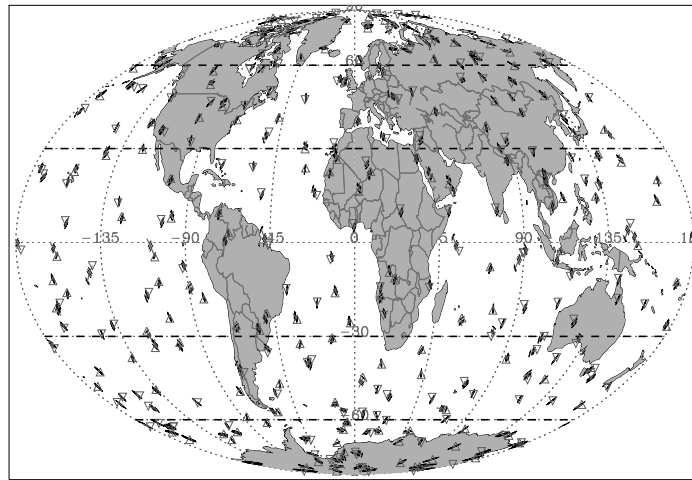


Fig. 1. Distribution of the 300 occultation events used in the study; rising occultations (triangles), setting occultations (upside-down triangles), latitude circles delimiting selected latitude bands (heavy dashed lines).

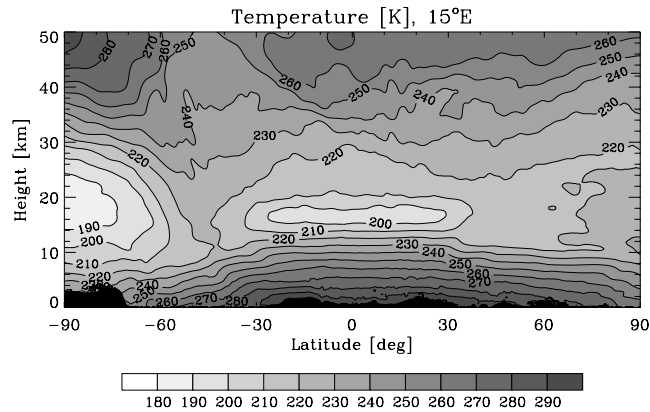


Fig. 2. ECMWF analysis field of September 15, 1999, 12 UT: temperature slice at 15°E.

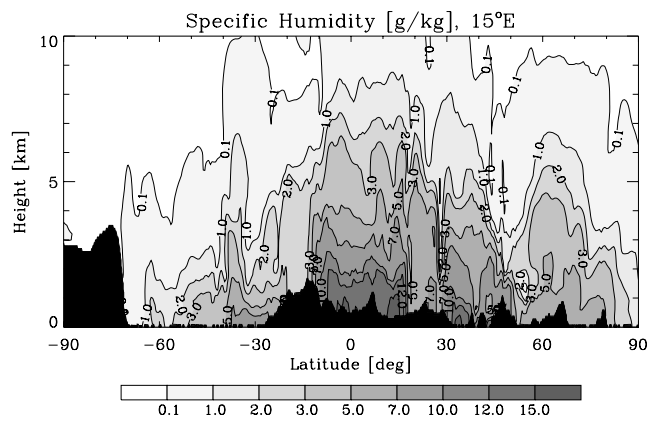


Fig. 3. ECMWF analysis field of Sept. 15, 1999, 12 UT: specific humidity slice at 15°E.

As atmospheric model we used the September 15, 1999, 12 UT, analysis field of the European Center for Medium-range Weather Forecast (ECMWF) with resolution T213L50 and the highest model level at 0.1 hPa (~ 60 km \times 60 km horizontal grid spacing, 50 vertical levels up to ~ 65 km height). This model resolution is capable of representing e.g., weather fronts, but smaller scale horizontal variations cannot be resolved. Figures 2 and 3 show exemplary slices of temperature and specific humidity, extracted from the analysis field, which indicate the quite realistic nature of the model. The ionosphere was prescribed with the NeUoG model, a global empirical 3D climatological model of the ionospheric electron density field (Leitinger et al. 1996).

3 Phase and Doppler Observables

Forward modeling of the signal propagation through the atmosphere-ionosphere system was performed with a sub-millimetric precision 3D ray tracer giving a signal profile as arriving at the sensor. Since raytracing stops at multipath situations in the lower troposphere in case of sharp vertical gradients this study does not include multipath and diffraction effects.

Observation system modeling was subsequently performed to superpose instrumental and the raw processing system effects on the forward modeled signal, including precise orbit determination (POD) errors, antenna pattern, local multipath, receiver thermal noise, and clock instabilities. The results are fairly realistic excess phase path profiles mimicking GRAS receiver performance.

Figure 4 illustrates, for the global ensemble (panel row a) and the selected latitude bands (panels rows b–d), the ionosphere corrected (LC) phase path profiles (left column). An occultation event starting/ending at 90 km (0 sec) lasts ~1–2 min with a (neutral gas) delay of ~2 mm near the mesopause (~80 km/~4 sec; in Fig. 4 involving ionospheric residuals), ~20 cm near the stratopause (~50 km/~16 sec), and >20 m below the tropopause level (~15 km/~30 sec). The near surface delay (~1 km height) reaches ~0.7–2 km depending on the atmospheric humidity. The ionospheric residual after linear ionospheric correction of phases is of the order of a few centimeters which can be seen in the phase path profiles in the first few seconds of the occultation, especially in the mean profiles of the ensembles. The different latitudinal ensembles reflect the varying influence of the ionosphere, showing ionospheric residuals of up to ~1 cm at high latitudes increasing to ~10 cm at low latitudes.

Figure 4, furthermore, illustrates the phase errors (middle column) and associated Doppler errors (right column), which are shown without the ionospheric errors in order to explicitly depict the errors due to the GRAS receiving system specifications. The rms error of the LC phase sampled at 10 Hz is seen to be 2–3 mm at <30 sec (above the tropopause), reasonably reflecting GRAS-type performance. While absolute errors increase into the troposphere, relative rms errors are still <0.02% at these low heights. The Doppler shift exhibits an rms error of ~3 mm/sec above the tropopause. Also for the Doppler shift, relative errors are found <0.02% in the troposphere. Biases in both, phase delay and Doppler shift, are negligible, reflecting the self-calibrated nature of these basic observables.

4 Retrieval and Error Analysis Scheme

We applied the ionospheric correction of bending angles, which leads to a considerably smaller residual bias on derived bending angles than the phase correction. The retrieval of atmospheric profiles involved an inverse-covariance-weighted statistical optimization of observed bending angles and best-fit MSIS (Hedin, 1991) model bending angles and, in general, the geometric optics retrieval scheme described by Gobiet and Kirchengast (2004). In the troposphere, an optimal estima-

tion retrieval algorithm (“1D-Var”, Healy and Eyre 2000) was applied to refractivity, using the ECMWF 24-hour short-range forecast for September 15, 1999, 12 UT, as background field for temperature and humidity. We retrieved bending angle, refractivity, pressure, geopotential height, temperature and specific humidity profiles for the full ensemble of profiles illustrated in Fig. 4 and empirically analyzed the errors of each retrieval product as follows.

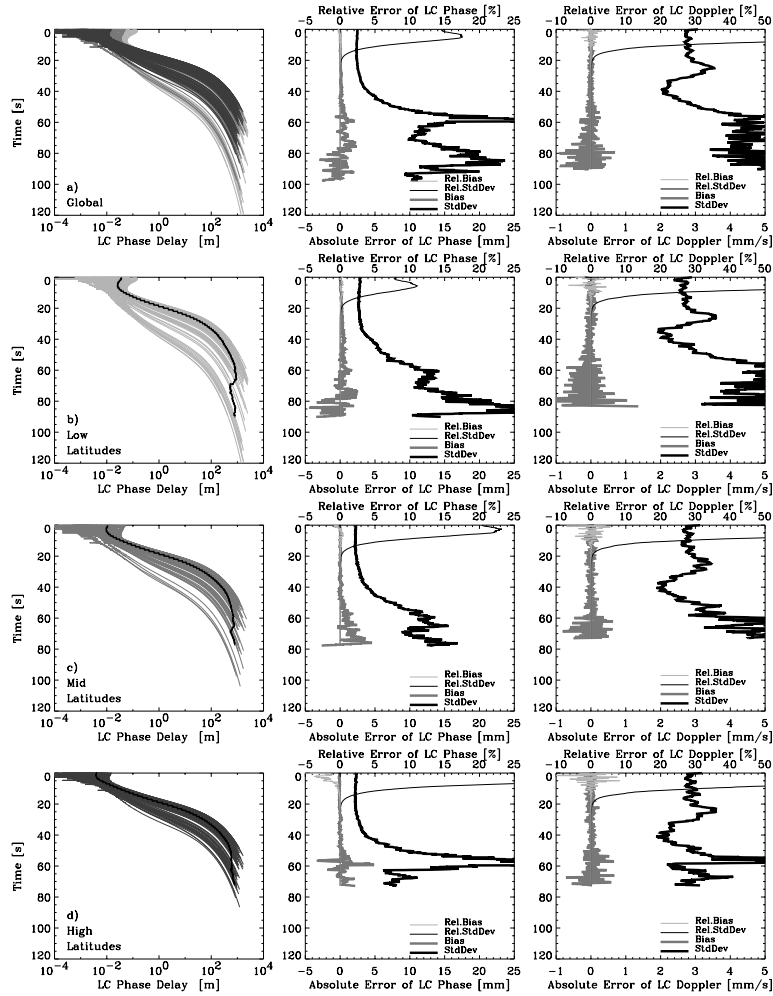


Fig. 4. The left panels show the ionosphere corrected LC excess phase path for the global ensemble (a) and the latitudinal ensembles (b–d); as well as the mean profile of each ensemble (heavy black line). The middle and right panels show the associated absolute (heavy) and relative (light) bias (grey) and standard deviation (black) of the LC phase delay and Doppler shift, respectively.

We computed the co-located vertical ECMWF profiles at a fixed mean tangent point location and defined it as the truth. This implies that our error estimates represent an upper bound error estimate including the observation error and the representativeness error, the latter becoming important in the lower troposphere due to horizontal variations (Foelsche and Kirchengast 2004; Syndergaard et al. 2004).

The difference profiles $\Delta\mathbf{x}$ ($\Delta\mathbf{x} = (\Delta x_1, \Delta x_2, \dots, \Delta x_i)^T$, with i denoting the height levels and T the matrix transpose) of the retrieved profiles (\mathbf{x}^{retr}) and the “true” profiles (\mathbf{x}^{true}) were calculated at an ECMWF-type L60 vertical grid in the form

$$\Delta\mathbf{x} = (\mathbf{x}^{retr} - \mathbf{x}^{true}). \quad (4.1)$$

Calculation of the mean of the difference profiles leads to the bias profile, \mathbf{b} ,

$$\mathbf{b} = \left[\frac{1}{n} \sum_{k=1}^{k=n} \Delta\mathbf{x}_k \right], \text{ with } n = \text{number of events in the ensemble.} \quad (4.2)$$

Next, the bias was subtracted from each profile giving bias-free profiles, $\Delta\mathbf{x}^{biasfree}$,

$$\Delta\mathbf{x}^{biasfree} = \Delta\mathbf{x} - \mathbf{b}. \quad (4.3)$$

From these bias-free profiles we computed the error covariance matrix, \mathbf{S} ,

$$\mathbf{S} = \left[\frac{1}{n-1} \sum_{k=1}^{k=n} (\Delta\mathbf{x}_k^{biasfree})(\Delta\mathbf{x}_k^{biasfree})^T \right], \quad (4.4)$$

with its diagonal elements representing the variances (S_{ii}) at height level i and with its non-diagonal elements representing the covariances (S_{ij}) between height levels i and j . The square root of its diagonal gives the standard deviation profile, \mathbf{s} ,

$$\mathbf{s} \text{ with } s_i = \sqrt{S_{ii}}. \quad (4.5)$$

The root mean square error profiles (**rms**) then reads

$$\mathbf{rms} \text{ with } rms_i = \sqrt{b_i^2 + s_i^2}. \quad (4.6)$$

The error correlation matrix, \mathbf{R} , with its elements R_{ij} denotes the error correlation between Δx_i at height i and Δx_j at height j . It is calculated by dividing the covariances S_{ij} by the square root of the product of variances S_{ii} and S_{jj} ,

$$\mathbf{R} \text{ with } R_{ij} = \frac{S_{ij}}{\sqrt{S_{ii} S_{jj}}}. \quad (4.7)$$

5 Results

We present, as examples, refractivity (Fig. 5) and temperature (Fig. 6) error estimates for the global (panels a) and latitude-band (panels b–d) ensembles up to ~50 km height. The left small panels show the number of events entering the statistics at a given height, with the bottom height set by requiring ≥ 10 ensemble members. The middle panels illustrate the error characteristics in terms of absolute and/or relative bias, standard deviation, and rms profiles. The relative quantities (units %) were computed by dividing the absolute quantities by the mean of the true profiles and multiplying with 100. The right panels display correlation functions, which are discussed in connection with Fig. 7.

Refractivity exhibits a relative standard deviation of 0.1–0.75% and a relative bias of <0.1% at 5–40 km height. Outside this “core” domain, the relative bias reaches 0.3% in the lower troposphere at all latitudes and up to 0.7% at 50 km height at high latitudes. The relative standard deviation stays below 2% outside the “core” domain, except for the low latitude ensemble, where it reaches 2.3% at the bottom.

Temperature shows a standard deviation of 0.2–1 K at 3–31 km height and a bias of <0.5 K below 33 km and of <0.1 K below 20 km for the global ensemble. In the lower troposphere, the standard deviation stays within 1.5 K in all latitude bands as a result of applying the 1D-Var retrieval algorithm. The temperature bias is lowest at mid latitudes with <0.1–0.2 K at 2–40 km. Large temperature errors occur at high latitudes, revealing a bias of >3 K and a standard deviation of >5 K above 40 km, which is reflected in the global error statistics and is mainly due to inadequate a priori profiles in this region (Gobiet and Kirchengast 2004).

Figure 7 depicts, for the global ensemble, the error correlation functions of all retrieval products for three height levels (~40 km, ~20 km, ~5 km) representative of upper stratosphere, lower stratosphere, and troposphere (for humidity three representative tropospheric levels are used). These functions express the correlation of errors at these heights with the errors in the remainder of the profile. The error correlation functions are defined as the rows of the error correlation matrix \mathbf{R} (Eq. 4.7).

Bending angle correlation functions show a sharp peak, while refractivity correlation functions are already broader, revealing the effect of the Abelian integration. The broadening in the troposphere seen in the refractivity error correlation functions is mostly a result of the errors due to horizontal variations. This broadening is not seen in the bending angle correlation functions since we computed the true bending angle by Abel transform from the true refractivity assuming spherical

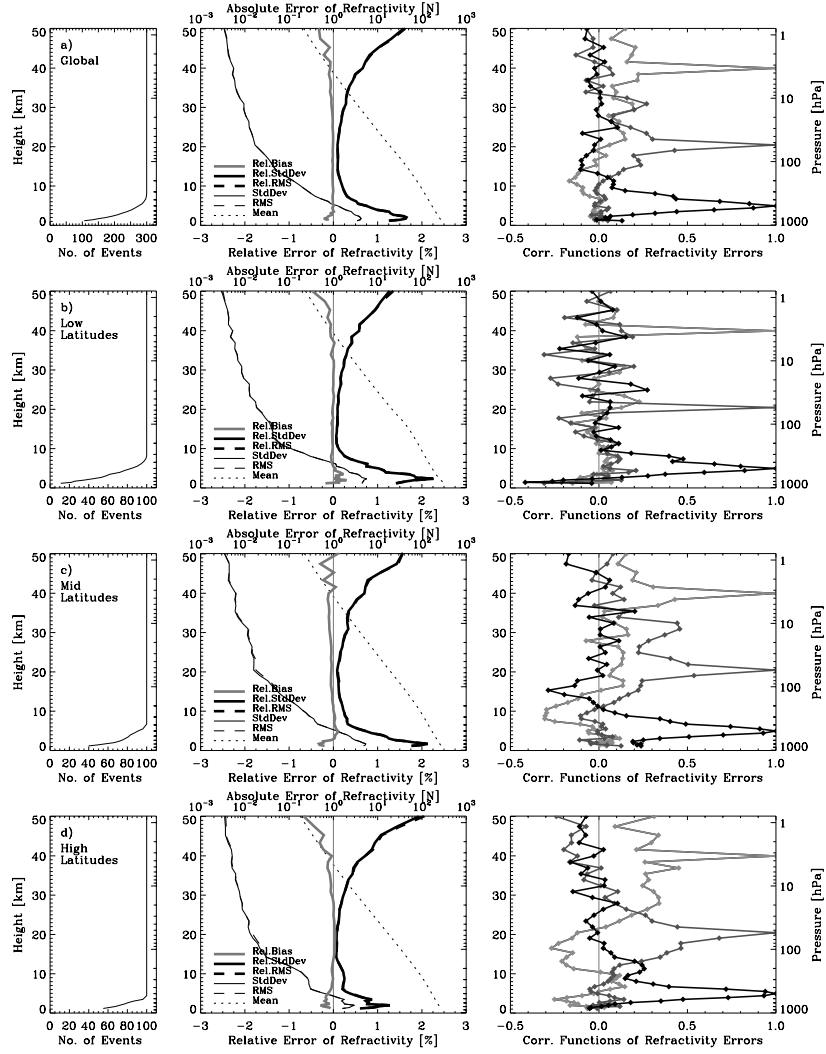


Fig. 5. Refractivity error analysis results for the global (a) and the latitudinal (b–d) ensembles. Left panels: number of events used for the error statistics calculation at any given height. Middle panels: relative bias (heavy grey), relative standard deviation (heavy black), relative rms (heavy black dashed) as well as the absolute standard deviation (light black), absolute rms (light dashed), and the mean of the “true” profiles (dotted). Right panels: error correlation functions for ~40 km (light grey), ~20 km (dark grey), and ~5 km (black) height, representative of upper stratosphere, lower stratosphere, and troposphere, respectively.

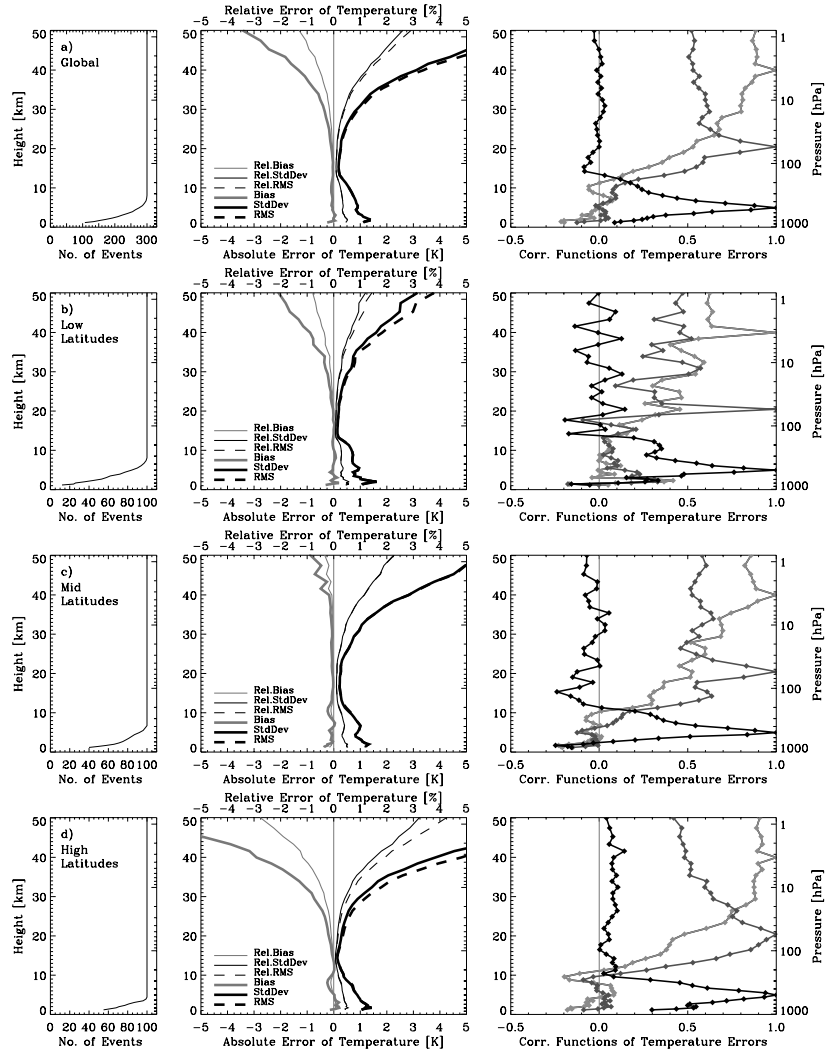


Fig. 6. Temperature error analysis results for the global (a) and the latitudinal (b–d) ensembles. Left panels: number of events used for the error statistics calculation at any given height. Middle panels: absolute bias (heavy grey), absolute standard deviation (heavy black), and absolute rms (heavy black dashed) as well as relative bias (light grey), relative standard deviation (light black), and relative rms (light black dashed). Right panels: error correlation functions for ~40 km (light grey), ~20 km (dark grey), and ~5 km (black), representative of upper stratosphere, lower stratosphere, and troposphere, respectively.

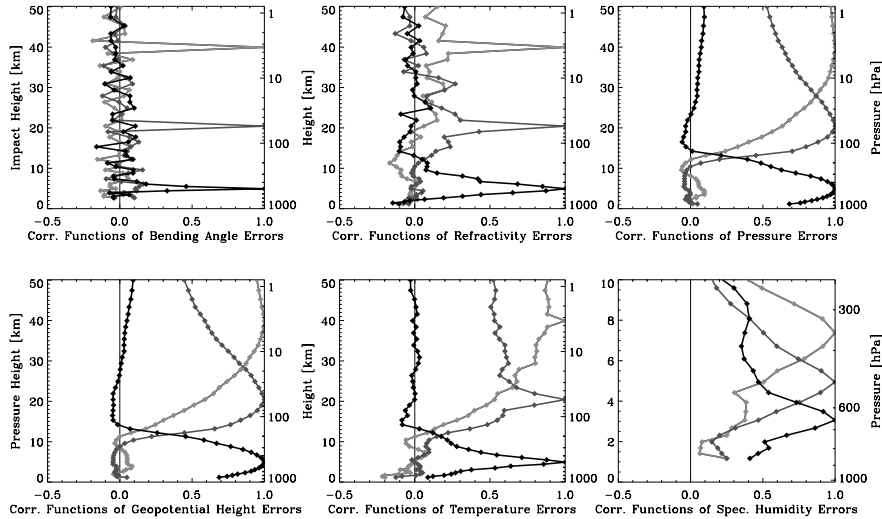


Fig. 7. Error correlation functions for three height levels, ~ 40 km (light gray), ~ 20 km (dark grey), and ~ 5 km (black), representative of upper stratosphere, lower stratosphere, and troposphere, respectively. The functions for all six retrieval products bending angle, refractivity, pressure, geopotential height, temperature, and specific humidity are shown (note the different height scale for specific humidity).

symmetry. While this still leads to reasonable results in the stratosphere it does not represent the errors under significant horizontal variations at full adequacy below ~ 7 km (Foelsche and Kirchengast 2004). This has to be taken into account when interpreting and using the bending angle error results.

Negative correlations in the bending angle and in refractivity stemming from derivative operations (Syndergaard 1999) are most pronounced in the low latitude ensemble at lower to middle stratospheric heights showing values of about -0.4 . Since the error statistics is performed on an L60 height grid these anti-correlation features are smoothed and can hardly be seen in the present plots but can be resolved on a finer, e.g., L90, grid.

Pressure and geopotential height errors exhibit strong correlation of errors due to the hydrostatic integration, the error correlation functions for geopotential height being basically the same as for pressure (cf. also Syndergaard 1999). Temperature correlation functions reveal both, pressure and refractivity correlation, being most akin to refractivity, where the pressure error correlation is smallest. Humidity errors show correlation function widths similar to temperature (note the different height scale). Humidity forms, together with temperature, the 1D-Var retrieval output and the main reason for the narrow correlation functions at tropospheric altitudes is related to the 1 D-Var retrieval applied below 15 km.

6 Conclusions

Overall, the results of this ensemble-based empirical error analysis are consistent with the findings in theoretical studies (Syndergaard 1999; Rieder and Kirchengast 2001). However, when comparing and interpreting them in relation to the findings in the theoretical studies one has to be aware of several differences between the studies. Whilst the theoretical studies dealt with unbiased errors and dry air retrievals, the present study includes horizontal variations and moist air retrieval. Furthermore, the theoretical studies discussed error characteristics of one profile or “Monte Carlo derived” profiles while this study looks at the statistics of an ensemble of profiles simulated under fairly realistic conditions.

The present error estimates are thus more generally applicable and expand and consolidate the rms error estimates obtained by Kursinski et al. (1997) based on a more simplified analysis. The empirically derived relative standard deviations of refractivity and temperature agree well with the rms errors estimated by Kursinski et al. (1997) in the upper troposphere to lower stratosphere; in the lower troposphere refractivity we found a twice as large error due to the more realistic horizontally variable fields used in the present analysis. Kursinski et al. (1997) also looked into error budget components not addressed here. An error budget analysis for a GRAS-type receiving system was recently performed by Ramsauer and Kirchengast (2001).

A key outcome of this study is the reasonable estimation of biases, available thanks to the realistic end-to-end modeling, especially for evaluating the climate monitoring utility of the data and for pin-pointing further improvement potential in the retrieval algorithms. The bias errors are most pronounced in the upper stratosphere, where they contribute appreciably to the total rms. For refractivity, the bias contribution has an impact on rms above 40 km, whereas for temperature this impact depends largely on latitude going down to as low as 20 km height at high latitudes. This result was, for example, already used as indicator of improvement potential by Gobiet and Kirchengast (2004), who then developed a further enhanced bending angle retrieval scheme, which leads to significantly smaller biases, especially at high latitudes.

Regarding error correlation functions, the main differences between empirically estimated ones and the theoretical ones are seen in the troposphere, including broader refractivity error correlation functions due to horizontal variability and relatively narrow correlation functions of temperature and humidity due to the 1 D-Var retrieval. Negative correlations can be hardly resolved on the L60 vertical grid. Nevertheless, they are present and most pronounced at stratospheric heights especially at low latitudes where they are comparable to the error correlation features in the theoretical studies (Syndergaard 1999; Rieder and Kirchengast 2001).

The conservatively estimated error covariance matrices are useful for evaluation and proper specification of observational errors in data assimilation systems and also provide a valuable basis for further retrieval algorithm improvements, e.g., in the 1D-Var retrieval part. In on-going work we derive simple analytical formulations of the refractivity error covariance matrices, closely fitting the em-

pirically estimated matrices, and with the degree of freedom to scale the error magnitude (standard deviation) to other than GRAS-type performance. These simple matrices will be convenient for use also in large-scale operational data assimilation systems.

Acknowledgements. The authors gratefully acknowledge valuable discussions on the topic with A. Gobiet (IGAM, Univ of Graz, Austria) and X.-Y. Huang (DMI Copenhagen, Denmark). U. Foelsche (IGAM, Univ of Graz, Austria) is thanked for the preparation of Figures 2 and 3. They also thank S. Syndergaard (Univ of Arizona, Tucson, USA) for fruitful discussions and his thorough review of the paper. A.K.S. was funded for this work from the START research award of G.K. financed by the Austrian Ministry for Education, Science, and Culture and managed under Program Y103-CHE of the Austrian Science Fund.

References

- Foelsche U, Kirchengast G (2004) Sensitivity of GNSS radio occultation profiles to horizontal variability in the troposphere: A simulation study. OPAC-1 Springer Proc Book, this issue
- Gobiet A, Kirchengast G (2004) Advancement of GNSS radio occultation retrieval in the upper stratosphere. OPAC-1 Springer Proc Book, this issue
- Healy SB, Eyre J (2000) Retrieving temperature, water vapour and surface pressure information from refractive index profiles derived by radio occultation: A simulation study. *Q J R Meteorol Soc* 126: 1661–1683
- Hedin AE (1991) Extension of the MSIS thermosphere model into the middle and lower atmosphere. *J Geophys Res*, 96: 1159–1172.
- Kirchengast G (1998) End-to-end GNSS Occultation Performance Simulator overview and exemplary applications. *Wissenschaftl Ber 2/98*, IGAM, Univ of Graz, Austria, 138 pp
- Kirchengast G, Fritzer J, Ramsauer J (2002) End-to-end GNSS Occultation Performance Simulator version 4 (EGOPS4) software user manual (overview and reference manual). Tech Rep ESA/ESTEC-3/2002, IGAM, University of Graz, Austria, 472 pp
- Kursinski ER, Hajj GA, Schofield JT, Linfield RP, Hardy KR (1997) Observing Earth's atmosphere with radio occultation measurements using the Global Positioning System. *J Geophys Res* 102: 23429–23465
- Leitinger R, Titheridge JE, Kirchengast G, Rothleitner W (1996) A “simple” global empirical model for the F layer of the ionosphere (in German; English version avail. from the authors). *Kleinheubacher Ber* 39: 697–704
- Ramsauer J, Kirchengast G (2001) Sensitivity of atmospheric profiles retrieved from GNSS radio occultation data to instrumental errors. Tech Rep ESA/ESTEC-6/2001, IGAM, University of Graz, Austria, 62 pp
- Riederer MJ, Kirchengast G (2001) Error analysis and characterization of atmospheric profiles retrieved from GNSS occultation data. *J Geophys Res* 106: 31755–31770
- Syndergaard S (1999) Retrieval analysis and methodologies in atmospheric limb sounding using the GNSS radio occultation technique. DMI Sci Rep 99-6, Danish Meteorol. Inst., Copenhagen, Denmark, 131 pp
- Syndergaard S, Flittner D, Kursinski R, Feng D, Herman B, Ward D (2004) Simulating the influence of horizontal gradients on retrieved profiles from ATOMS occultation measurements – a promising approach for data assimilation, OPAC-1 Springer Proc Book, this issue